AIAA JOURNAL
Vol. 44, No. 12, December 2006

Characterizing Laser-Generated Hot Spots for Receptivity Studies

Terry R. Salyer
Los Alamos National Laboratory, Los Alamos, New Mexico 87545
and
Steven H. Collicott* and Steven P. Schneider
Purdue University, West Lafayette, Indiana 47907

DOI: 10.2514/1.13023

Simple, well-characterized experimental perturbations are needed to validate CFD simulations of supersonic and hypersonic boundary-layer receptivity. A laser-generated hot-spot perturbation has been characterized and modeled, based on experiments in the Purdue University Mach-4 quiet-flow Ludwieg tube. The model provides a detailed density profile and time evolution for the perturbation, which consists of a hot spot and the surrounding weak shock. The model is validated by comparing simulated optical path differences to measurements from a high-sensitivity, high-bandwidth laser differential interferometer. CFD simulations are compared with receptivity experiments on a hemisphere to illustrate the usefulness of the perturbation model.

I. Introduction

LAMINAR-TURBULENT transition is important for many high-speed vehicles [1]. In low-disturbance environments on reasonably smooth surfaces, transition is generally the result of the growth and breakdown of instability waves. The process by which freestream disturbances enter the shock layer and introduce instability waves is called *receptivity* [2]. Freestream disturbances at supersonic speeds can be analyzed in terms of vortical, acoustic, and entropy fluctuations [3]; all three types must be considered for a complete analysis, although each is converted into all types upon passing through a bow shock [4]. Because all real vehicles have bow shocks, analyses without bow shocks would seem to have limited applicability.

Although considerable progress has been made for low-speed receptivity to acoustic waves, supersonic receptivity is not well understood, particularly on blunt bodies. Experimental work began with acoustic disturbances, probably because these are easier to generate [5]. The acoustic disturbances were generated by radiation from a localized glow perturber on a secondary plate. Although these give a simple pure frequency, the spatial distribution of amplitude and phase has a complex three-dimensional pattern that is not simple to analyze. Egorov et al. [6] have done much to develop the theory for acoustic disturbances, and Zhong [7] has developed our understanding via direct numerical simulations. Several of the papers from Zhong's group have included blunt bodies and even high-enthalpy effects [8].

Disturbances in entropy and vorticity must also be considered if receptivity is to mature toward engineering utility, because all forms may exist in ground and flight experiments [9]. The localized laser-induced hot spot was developed as a feasible alternative to acoustic waves, for controlled receptivity experiments [10]. Hussaini and Erlebacher [11] performed two-dimensional and axisymmetric numerical simulations of localized spots interacting with shock waves. However, they were forced to assume an arbitrary shape for the initial disturbance. Fabre et al. [12] analyzed the interaction of a cylindrical entropy spot with a shock, assuming a Gaussian spot and working in two dimensions. Federov and Tumin [13] considered receptivity to a localized two-dimensional disturbance in Mach-6 flow past a cone. Again, they were forced to assume an arbitrary initial disturbance and were limited to two space dimensions.

Transition on blunt bodies is important for missiles and other devices, yet current understanding is limited by the "blunt body paradox," which refers to the paradoxical early onset of transition and high turbulent heat transfer within the boundary layer of a blunt body in supersonic flow [14]. Transition has been found to occur at a Reynolds number an order of magnitude lower than that predicted by instability theory on polished cold-wall heat-sink noses. Although some believe that the early transition can be explained by surface roughness, others do not, and the issue remains controversial. Morkovin [15] investigated the processing of upstream disturbances by the bow shock, seeking evidence of disturbance growth within the subsonic region, but found no amplification within his one-dimensional linear theory. Spatially periodic structures in the subsonic region of a blunt model have also been observed in some curious shadowgraphs that have yet to be explained [16].

The work reported here extends experimental efforts dating back to 1996 [17], in which controlled laser-induced perturbations convected into the nose of a hemisphere and generated fluctuations were measured with a high-frequency pressure transducer. A computational model of these early experiments was developed by Dunn [18], who computed the unsteady bow-shock disturbance interactions in Mach-4 flow past a hemisphere. Dunn's direct Navier–Stokes simulation modeled the perturbation as an energy pulse on the stagnation streamline. The results suggest the generation of both pressure waves and vortex rings within the subsonic region, where the pressure waves are dependent on the energy of the hot spot. Resonance (damped pressure waves) within the subsonic region (like that found in the experiments [17,19]) was not confirmed, possibly due to insufficient resolution in the simulation [18]. However, the pressure amplitudes and the general shape of the time-history resemble the experimental observations.

Improved instrumentation was necessary for investigating the high-speed blunt body receptivity problem, because the high-frequency pressure measurements were contaminated by diaphragm ringing. Therefore, calibrated phase measurements were made using a laser differential interferometer (LDI) (Fig. 1) [19,20].

A. Past LDI Receptivity Experiments

Although the calibrated data from the receptivity experiments are useful for direct comparison with CFD results, comparing CFD with

Presented as Paper 3230 at the 22nd AIAA Aerodynamic Measurement Technology and Ground Testing Conference, St. Louis, Missouri, 24–26 June 2002; received 23 September 2004; revision received 26 September 2006; accepted for publication 27 September 2006.

*Corresponding Author, School of Aeronautics and Astronautics.

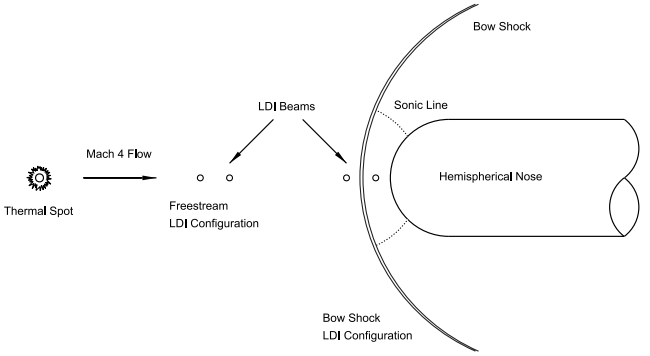

Fig. 1 Test flow configuration with blunt body.

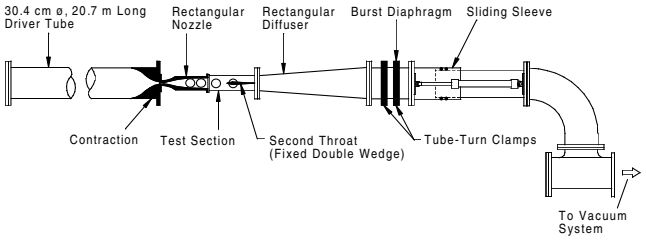

Fig. 2 Sketch of Purdue University Mach-4 quiet-flow Ludwieg tube.

the experiment can be difficult when computationally derived quantities (such as temperature and density) differ from measured flow quantities (as determined by optical path differences from the LDI). This work describes how to connect CFD simulations and experimental LDI data in supersonic flows involving a controlled, repeatable hot-spot perturbation.

The first part of this paper describes a numerical simulation of the LDI characterization of the hot spot in the freestream. This simulation is used to determine (with experimental validation) the time-varying density profile of the laser-generated hot spot. The second part describes a method of code validation and is illustrated using a DNS simulation by Dunn [18]. The results from the analysis of Dunn's data are compared with the experimental LDI data.

A repeatable, controlled perturbation in the form of a laser-generated hot spot was used to create a disturbance within the subsonic region behind the bow shock of a 1-in.-diam hemisphere-cylinder model [19,20]. The perturbation was introduced upstream of the model and convected downstream at Mach 4 to impinge on the detached bow shock, as shown in Fig. 1. The LDI was used to analyze both the hot spot in the freestream and the effect that it had on the subsonic region at the nose of the model. Schlieren imagery and simultaneous Kulite pressure measurements at the nose of the model supplement the LDI measurements. The effects of transition mechanisms other than bluntness were reduced in these experiments through use of a highly polished model, low freestream pressure fluctuations, and filtered driver air.

II. Experimental Facility

Measurement of perturbations and small amplitude disturbances in boundary layers requires a facility with uniform, quiet-flow conditions in the test section. The Purdue University Mach-4 quiet-flow Ludwieg tube (shown in Fig. 2) is a low-noise facility that provides excellent flow conditions for such measurements [21]. The facility is considered to generate quiet flow [21–24], because the root mean square pressure fluctuations during a run are approximately 0.05% of the mean pressure, for an initial total driver pressure of $1.01\text{E}+05$ Pa and a total temperature of $2.95\text{E}+02$ K. The flow in the tunnel is quasi steady, typically lasting approximately 3.5 s. The drop in pressure due to the passage of the first expansion wave is approximately 1.2% of the initial total pressure behind the bow shock after quiet flow is established. Through a series of 0.1-s expansion wave cycles, the stagnation pressure decreases in steps by approximately 35% throughout the run, whereas the stagnation temperature decreases by approximately 10%. Computed flow quantities [19] (from measured pressure and temperature) for four points (each 10 expansion cycles apart) throughout a typical run with a driver pressure of $6.76\text{E}+04$ Pa and driver temperature of $2.98\text{E}+02$ K (the same conditions as the experiments) are listed in Table 1.

A. Controlled Perturbation

Short, high-energy pulses of light from an injection-seeded, frequency-doubled Nd:YAG laser are focused into the test section upstream of the model to create a small hot spot [19,20]. The laser is typically operated at a pulse rate of 10 Hz. Initially, the process creates a small ball of plasma surrounded by an expanding shock wave by photoionizing the air in the test section [20,25]. The plasma then quickly reassociates and leaves a local hot spot surrounded by an expanding weak shock. This hot spot then convects downstream to be used as a repeatable, controlled perturbation. Laser pulse energies were around 230 mJ per 7 ns pulse at a wavelength of 532 nm. The optical system is shown in Fig. 3.

B. Laser Differential Interferometer

The laser differential interferometer (LDI) provides unique measurement capabilities especially suited for low-density flow diagnostics [26,27]. With high-sensitivity, large bandwidth, and small spatial resolution, the LDI is able to measure weak perturbations in low-density flow [19,20]. The basic system [20] and the feedback stabilized system [19] are capable of detecting wavelength shifts as low as $\lambda/13,000$ at bandwidths up to 6 MHz (0.5 dB signal drop). The spatial resolution is 0.1 mm normal to a line through the flow and is integrated along that line [28]. With the basic system, the phase shift is limited to approximately 10% of a wavelength to remain within the calibrated linear portion of the device. The feedback-stabilized LDI with active phase compensator broadens the useful range of the system to half of a wavelength. This active phase compensation was necessary for acquiring calibrated data from the bow-shock receptivity experiments [19].

The basic LDI system sends two closely spaced beams through the test section and then recombines and interferes the beams on a pair of photodetectors, as shown in Fig. 4. The system detects the rapid phase shift between the two beams. Calibration is simple and quantitative phase shifts are easily determined. Small optical path

Table 1 Ludwieg tube flow parameters at four times during a typical run.

Quantity	0.3 s	1.3 s	2.3 s	3.3 s
P_o, psia	$9.41\text{E}+00$	$8.13\text{E}+00$	$7.08\text{E}+00$	$6.23\text{E}+00$
P_o, Pa	$6.49\text{E}+04$	$5.61\text{E}+04$	$4.88\text{E}+04$	$4.30\text{E}+04$
P, Pa	$4.27\text{E}+02$	$3.69\text{E}+02$	$3.22\text{E}+02$	$2.83\text{E}+02$
T_o, F	$7.12\text{E}+01$	$5.28\text{E}+01$	$3.54\text{E}+01$	$1.97\text{E}+01$
T_o, K	$2.95\text{E}+02$	$2.85\text{E}+02$	$2.75\text{E}+02$	$2.66\text{E}+02$
T, K	$7.02\text{E}+01$	$6.78\text{E}+01$	$6.55\text{E}+01$	$6.34\text{E}+01$
ρ_o, kg/m^3	$7.67\text{E}-01$	$6.87\text{E}-01$	$6.19\text{E}-01$	$5.63\text{E}-01$
ρ, kg/m^3	$2.12\text{E}-02$	$1.90\text{E}-02$	$1.71\text{E}-02$	$1.56\text{E}-02$
V, m/s	$6.72\text{E}+02$	$6.60\text{E}+02$	$6.49\text{E}+02$	$6.38\text{E}+02$
Re_{cm}, cm^{-1}	$3.00\text{E}+04$	$2.74\text{E}+04$	$2.53\text{E}+04$	$2.35\text{E}+04$

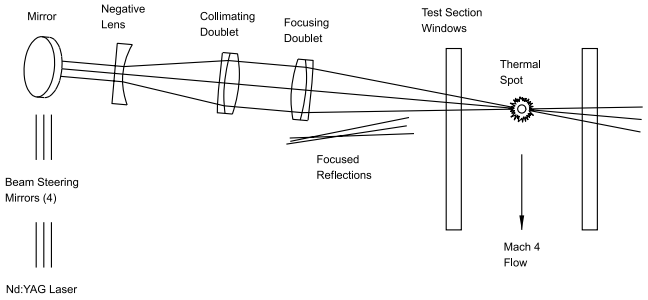

Fig. 3 Schematic of hot spot generation in Ludwieg tube.

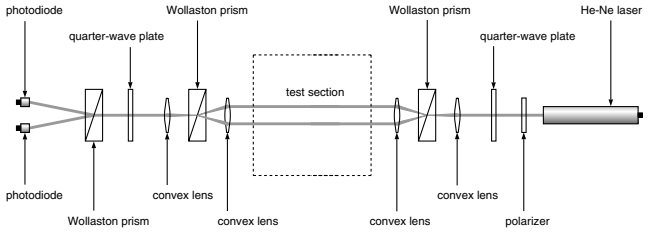

Fig. 4 Schematic of basic laser differential interferometer.

changes caused by a phase object in the test section lead to light intensity changes on the photodiodes and, hence, electrical signals in the photodiode circuitry. This relation is given by

$$\frac{\Delta E}{E_0} = \frac{\Delta U}{U_0} = \pi \frac{\delta \Phi}{\lambda} \tag{1}$$

or

$$\delta \Phi = \frac{\lambda}{\pi} \frac{\Delta E}{E_0} \tag{2}$$

where U is light intensity, E is voltage in the photodiode circuit, $\delta\Phi$ is the optical path length difference, and λ is the wavelength of the laser (632.8 nm). E_0 is the voltage calibration value measured before the experiment. The phase modulator (for feedback stabilization) can be added to the basic system. The phase modulator is inserted into the system after the second Wollaston prism and before the last quarter-wave plate (see the basic layout in Fig. 4). References [29,30] present more details of the LDI.

C. Characterization of Controlled Perturbation

Measurements of hot spots in the Purdue University Mach-4 quiet-flow Ludwieg tube can be found in [10,31,32]. Measurements of similar spots are reported by Yan et al. [25]. LDI measurements that show hot-spot amplitudes, spatial characteristics, and repeatability have also been presented [20]. The LDI measurements show a hot-spot diameter of approximately 5 mm and a weak shock radius of 8 mm when the hot spot hits the bow shock of the hemispherical model approximately 45μs after it is created. The weak shock is not detected in the hot-wire studies, although the width of the spot itself (based on half the maximum amplitude) was measured as approximately 5 mm [33].

The LDI detects the difference in the total optical path length along two lines through the disturbance. CFD results typically provide the dynamic density field $\rho(x, y, z, t)$. LDI measurements and CFD are compared using the line-integral optical path length (say, in the z direction), in a plane of constant y value $\Phi(x, t)$, where x is the position in the disturbance measured in the direction of the freestream and t is time. This quantity is one that is easily computed from both the density field produced by CFD and from the LDI data. In this case, it is useful to consider the absolute optical path length at a single location. This can be realized by a simple transform procedure.

Computation of Φ from the density field is described next. Computing Φ from the LDI signal $f(t)$ begins with the continuous time voltage signal from the LDI:

$$f(t) \propto \Phi(x, t) - \Phi(x + \Delta x, t) \tag{3}$$

$$f(t) \propto \Delta x \frac{\partial \Phi(x, t)}{\partial x} \tag{4}$$

where Δx is the beam spacing. Given that the perturbation flows through the measurement region at constant speed V, Eq. (4) is also

$$f(t) \propto \Delta x \frac{\partial \Phi(Vt, t)}{\partial x} \tag{5}$$

Integrating $\partial\Phi/\partial x$ in time is thus equivalent to integrating in x/V for a nonevolving disturbance (the evolving disturbance case is discussed next). The integral is

$$\int_0^t f(t_2)\, \mathrm{d}t_2 \propto \int_0^t \frac{\partial \Phi(Vt_2, t)}{\partial x}\, \mathrm{d}t_2 \tag{6}$$

$$\int_0^t f(t_2)\, \mathrm{d}t_2 \propto (1/V) \int_0^{Vt} \frac{\partial \Phi(x, t)}{\partial x}\, \mathrm{d}x \tag{7}$$

$$\int_0^t f(t_2) dt_2 \propto \Phi(t)/V \tag{8}$$

where t_2 serves as dummy variable for integration purposes and $\Phi = 0$ in the freestream. Note that the integration in x has reduced Φ to a function only of time. Thus, the time integral of the LDI signal produces the desired information about the line-integral optical phase delay through the perturbation. The phase delay along the centerline of the spot was computed in earlier work by the authors, in which they assumed that there is no evolution of the disturbance [20]. Although the shock grows rapidly, the inner hot spot grows slowly and is approximately constant in size during the duration of the measurement [19,20,33].

The optical characteristics along one plane through the volume occupied by the perturbation are described by $\Phi(x, t)$. The entire volume could be built up with data from numerous LDI beam pairs, but this is unnecessary for the present work. If the perturbation is axisymmetric, then an Abel inversion may be applied to determine the density field throughout the disturbance.

The assumption that the perturbation does not evolve permits Eq. (3) to be rewritten as

$$f(t) \propto \Phi(t - t_{\text{delay}}) - \delta\Phi(t) \tag{9}$$

where $t_{\text{delay}} \approx \Delta x/V$ and $\delta\Phi$ is the optical path length difference between the two beams. A modification of Eq. (9) is required to account for the time evolution of the shock propagating outward from the hot spot. A simple modification is chosen: t_{delay} is varied based on the speed of the weak shock wave. For instance, the shock leading the hot spot moves at approximately Mach 5 through the interrogation region, and so t_{delay} is decreased in that region. (Note that the Mach-5 value is the result of a Mach-4 spot convection speed plus roughly Mach 1 for the expanding lead weak shock front. These values are derived from the shock and spot arrival times in the raw LDI data.) Similarly, t_{delay} is increased for the slower-moving shock that trails the hot spot. An approximation must be made in choosing t_{delay}, because the velocity field of the air between the shock and the hot spot could not be measured. A constant time delay was used in the regions leading and trailing the hot spot and inside the shock. The corresponding time delays and integrated LDI responses using the variable time delay method [20] are shown in Fig. 5 for the four flow times of Table 1. Results of applying the variable time delay are shown in Fig. 6. Here, the results for four measurements are shifted to align the start of the weak shock propagating at Mach 5. The four curves show changes in the optical path along one line through the evolving perturbation rather than as the optical path difference between two lines through the perturbation. These results provide the

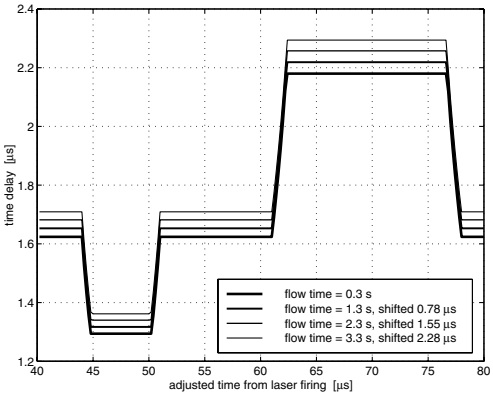

Fig. 5 Time delay variation for LDI response integration.

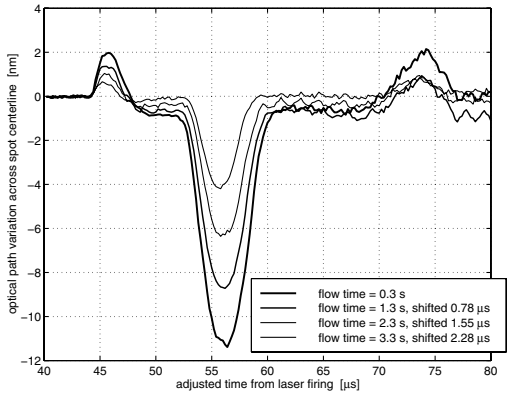

Fig. 6 Integrated LDI response using variable time delay method.

link between the experiment and the numerical simulation in the perturbation model.

III. Simulation of Controlled Perturbation

Because the perturbation evolves as it flows downstream, a simple numerical integration of the LDI response yields only the optical path variation vs time along a diameter of the spot. To determine the density profile of the hot spot, a numerical model is developed to simulate the growth of the hot spot and the surrounding weak shock, their motion downstream, and their passage through the beams of the LDI. The simulated LDI output and optical path variation across the spot are determined.

The goal of the simulation is to match the experimental results as closely as possible. By matching the simulated optical path variation with the measured optical path variation from the integrated experimental data, the density profile of the hot spot is inferred. With this knowledge, characterization of the hot spot used for the receptivity experiments is improved. In addition, the profile provides a realistic, experimentally justified input disturbance for use in CFD codes.

A. Model for Controlled Perturbation

In the model, detailed in [28], two formulas represent various portions of the perturbation. As discussed next, the perturbation consists of the hot-spot region, the shock region, and the middle region (see the inset of Fig. 7).

The first function models the shock region of the perturbation and is a modified inverse square law:

$$f = f_{\text{offset}} + \left[\frac{k_1}{k_{\text{mod}}}x + \frac{1}{\sqrt{f_0 - f_{\text{offset}}}}\right]^{-2} \tag{10}$$

where f is the quantity modeled (Mach number, radius, temperature, or index of refraction), x is the abscissa value (either a time or radial

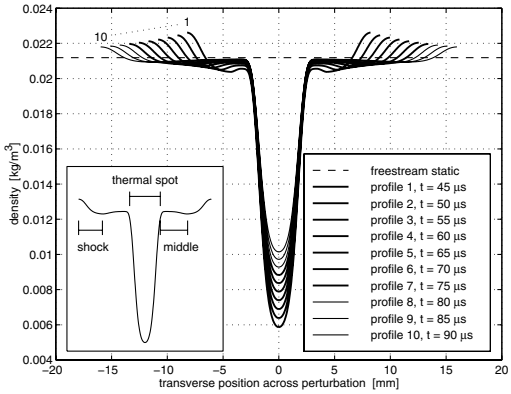

Fig. 7 Simulated density variation across the hot spot (including shock).

distance), f_0 is the maximum value at zero abscissa, f_{offset} is the offset that the function asymptotically approaches, k_1 is an attenuation factor, and k_{mod} is the attenuation modification factor. The value of k_1 is set by the spatial decay of the response near the shock with $k_{\text{mod}} = 1$. When this fails to produce a good fit to the data, then k_{mod} is altered to provide a good fit to the data. In these cases, k_{mod} is defined as

$$k_{\text{mod}} = (k_2 x + 1)^{-2} \tag{11}$$

where k_2 is the parameter that is set to achieve the fit.

The second function models the hot-spot region of the perturbation and is a modified Gaussian distribution, defined here as

$$f = \frac{1}{(\sigma/\sigma_{\text{mod}})\sqrt{2\pi}} \exp\left[-\frac{1}{2}\left(\frac{x-\mu}{(\sigma/\sigma_{\text{mod}})}\right)^2\right] \tag{12}$$

where f is the functional quantity determined (here, an index of refraction), x is the abscissa value (here, a radial distance), μ is the Gaussian mean (or translation of the peak), σ^2 is the Gaussian variance, σ_{mod} is the Gaussian variance modification factor, and σ is set by the width of the data in the region of the hot spot with $\sigma_{\text{mod}} = 1$. When necessary to achieve a good fit, σ_{mod} becomes a function of position:

$$\sigma_{\text{mod}} = 1 + kx^2 \tag{13}$$

where k is a parameter that is set to achieve a good fit to the data.

The hot spot is approximated as a sphere of hot gas with a modified Gaussian temperature distribution [as in Eq. (12)]. The modification [as in Eq. (13)] flattens the density variation near the center of the spot while allowing a steep dropoff near the "edge" of the hot spot. The model also allows the hot spot to grow asymptotically to a given size at which the growth is proportional to the inverse square of the simulation time [as in Eq. (10)]. The variance changes as a function of the hot spot radius, as well. This distribution was developed to match the LDI results.

The temperature difference within the hot spot (above freestream temperature) decreases proportionally to the inverse square of time, asymptotically approaching zero [as in Eq. (10)]. The maximum temperature differential and proportionality constant are set to match the experimental data. See Fig. 8 for a plot of the reduction in hot-spot temperature differential. It is apparent that the temperature differential of the spot drops from roughly 200 to 100 K as the hot spot passes through the LDI beams. Note that the simulation is only valid (experimentally justified) between 40 and 80 μs.

An approximation to Sedov's blast theory [34] is used to model the expanding weak shock outside of the hot spot. The peak strength of the shock diminishes proportionally to the inverse square of the shock radius [as in Eq. (10)], with a maximum shock strength and proportionality constant set to match experimental data. The shock Mach number asymptotically approaches unity as the shock weakens

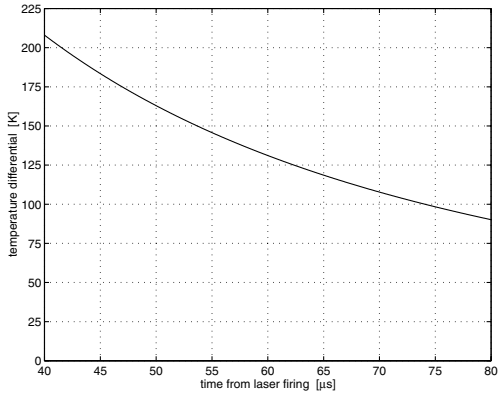

Fig. 8 Simulated reduction in hot spot temperature differential.

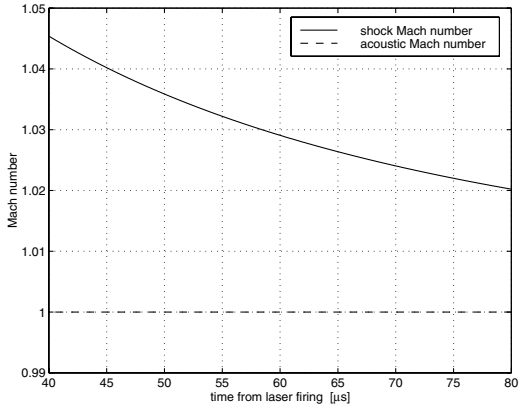

Fig. 9 Simulated reduction in shock Mach number.

to an acoustic disturbance in the far field. See Fig. 9 for a plot of the reduction in Mach number of the surrounding weak shock.

The density immediately behind the shock is computed from normal shock relations using the shock strength at that time. Within the shock region (see the inset of Fig. 7), the density drops off proportionally to the inverse square of the distance from the edge of the shock [as in Eq. (10)], approaching the density of the middle region. The middle region (see the inset of Fig. 7) is defined here as the region between the shock region and the edge of the hot spot at the core of the perturbation. The attenuation of the density profile within the shock region is also modified [as in Eq. (11)] to match experimental results.

The density in the middle region varies as a Gaussian spread [as in Eq. (12)] centered on the minimum at the inner edge of the shock region and increasing toward the edge of the hot spot. This density spread (variance) increases proportionally to the square of the middle-region radius. The minimum density at the inner edge of the shock region increases in time, asymptotically toward the freestream static density, proportionally to the inverse square of the shock radius [as in Eq. (10)]. This varying density determines the lower bound of an envelope for the middle region. The density at the edge of the hot spot (which is the continuity point between the hot spot and the outer regions) also increases, asymptotically approaching freestream static density, proportionally to the inverse square of the extent of the middle region [as in Eq. (10)]. Again, these distributions are developed from the LDI measurements of hot spots in the Purdue University Mach-4 quiet-flow Ludwieg tube. Source code from this implementation of the model is given as an appendix in [28].

B. Simulation Results

Inputs for the simulation include: the basic LDI parameters such as LDI beam spacing and location downstream from the perturbation initiation point, index of refraction reference values for the laser wavelength, the local freestream conditions, and various perturbation modeling parameters for the shock, hot spot, and middle region.

The simulation is a simple time-marching scheme. At each time increment, the evolution of the shock and hot spot is computed. When the expanding shock of the perturbation first reaches the LDI beams, the optical path length is computed along each LDI beam, here defined as

$$\text{optical path length} = \sigma_i = \int_{s_i} n(s,t)\,\mathrm{d}s = \int_{s_i} 1 + \beta\frac{\rho(s,t)}{\rho_s}\,\mathrm{d}s \qquad i = 1,2 \tag{14}$$

where $n(s,t)$ is the index of refraction, ρ_s is the reference density taken at standard conditions (0°C and 760 mm Hg), and $\beta = 0.000291$ for red light in air. After the optical path lengths are computed, the difference $\delta\Phi = \Phi_2 - \Phi_1$ is calculated. This is the quantity measured by the LDI.

Figures 7 and 10 depict the main result: the density variation across the controlled perturbation as it evolves through time. Figure 10 details the more complex shock region. Freestream static density is indicated in each plot. The thicker lines (profiles 1 through 7) indicate profiles during the period in which the perturbation intersects the LDI beams.

In agreement with the experiments, the model hot spot grows rapidly to approximately 5 mm in diameter within approximately 45 μs, corresponding to the instant for which results are plotted in Fig. 7. The shrinking magnitude of the shock and middle region clearly illustrates how the weak shock dies off in the far field. Looking at Fig. 10 again, the varying density field of the middle region indicates a dip in density near the edge of the shock region. Intuition might have suggested a flat density profile in the middle region, but the specified profile is necessary for the simulation results to approximate the experimental results.

In Fig. 11, contours of the perturbation density field are presented for four times during the intersection of the spot with the LDI beams, as the perturbation evolves before impinging on the bow shock. The LDI beam spacing used for the freestream studies was 1.1 mm.

To match the numerical simulation with the experimental results, the optical path variation across the perturbation centerline was computed and compared with the same quantity from the (line-integral) experimental data. In practice, tuning the model to match the experimental LDI results is more intuitive when working with absolute optical path variations. In addition, insight is gained into the physical parameters that govern the spot formation. Figure 12 shows the modeled optical path variation for both LDI beams and the experimental results of Fig. 6 (plotted again in Fig. 12), in which it is noted that the central peak magnitudes differ by only 1.3%.

Finally, Fig. 13 illustrates the agreement between the model and the experimental results. Note that two sets of experimental results are shown superimposed on the numerical results. The shock arrival and departure times, as seen by the LDI, are modeled with 1% timing accuracy. The hot-spot magnitude is within 2.2% of the experimental

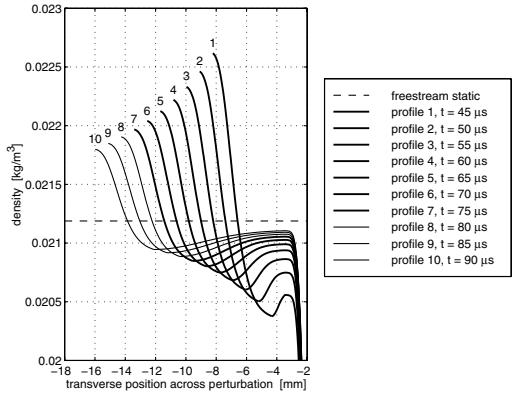

Fig. 10 Simulated density variation across the shock.

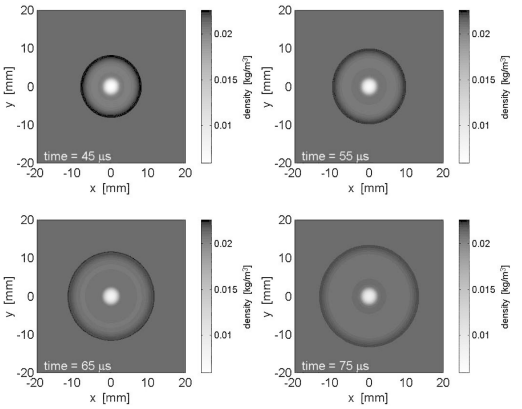

Fig. 11 Simulated density variation across the hot spot (including shock).

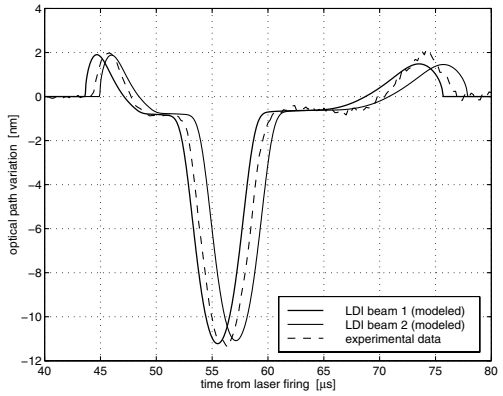

Fig. 12 Simulated optical path variation across the hot spot (including shock).

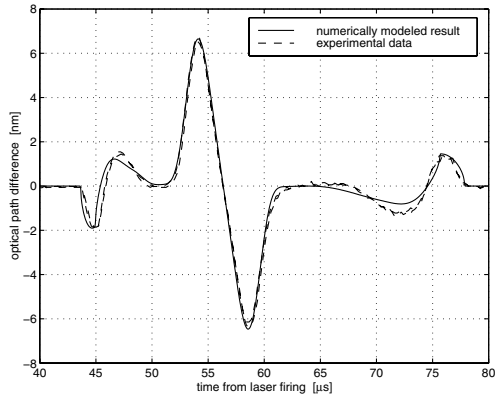

Fig. 13 LDI response to passage of the hot spot (including shock).

data, and the shape is a near match. Even within the shock and middle region, the measurements and simulation agree with an average of 6.9% difference in peak amplitudes. If a better theoretical approach is taken to help determine the proper representation of these regions, even better results might be acquired.

IV. Comparison with CFD Results

With the improved model of the perturbation described previously, better comparison between CFD simulations and measurements of unsteady hypersonic flows are possible. However, to compare CFD data with the earlier experimental results [19,20], a method to generate comparable flow quantities from CFD data is required. As an example, data from Dunn [18] are used to compare with LDI measurements by propagating simulated LDI beams through the CFD density field.

Dunn [18] solved the Reynolds-averaged Navier–Stokes equations to compute a time-accurate finite volume simulation of the unsteady flowfield around the nose of the hemisphere-cylindrical model perturbed by a hot spot of an assumed form. A Steger-–Warming flux-splitting scheme with upwind-biased differencing was used to capture the shock. The duration of the simulation was 117 μs.

Using the time-varying density field around the model, a simulated LDI output was computed. First, the density data were extracted from the curvilinear grid by interpolating the data at equally spaced points along lines representing the LDI beam paths. Six LDI beam pair locations were chosen to match the measurement locations in the experiment. Five locations at $x = 0.1$, 0.6, 1.1, 1.6, and 2.1 mm are within the bow shock, where x is measured upstream from the stagnation point on the hemispherical nose. The sixth location at $x = 2.6$ mm is just upstream of the bow shock and thus represents the freestream data. The reference beam of each LDI beam pair is located 7.4 mm upstream of its partner, well upstream of the bow shock. After the density data were extracted along these beam paths in the CFD result, the optical path length along each beam was computed using Eq. (14). The optical path difference was then compared with the output of the LDI for each measurement location.

The optical path length of a beam running through the relatively high-density region behind the bow shock will be much longer than the optical path through the freestream flow. To compensate for this in the experiment, a feedback-stabilized LDI was used with an electrooptic phase modulator to automatically remove this large offset [19]. The perturbation-induced fluctuations within the subsonic region were not affected by the phase modulator. In contrast, removal of this steady bow-shock region offset was simple for the density data from CFD. First, the difference in optical path lengths between beams in a given pair was computed before the perturbation impinged on the bow shock. Then, this value was subtracted from the optical path difference for this given beam pair throughout the rest of the simulation. Thus, the optical path difference was zero before the perturbation impinged on the bow shock, just as in the experiment. Figure 14 depicts the bow-shock offset and how it varies at the different measurement locations. The half-wavelength of the LDI interrogation laser is also plotted. This is the maximum phase offset that could be removed by the phase modulator.

Obviously, in the CFD simulation, the maximum phase offset for $x < 1.2$ mm is too large for the LDI to tolerate. Note that the results computed by Dunn [18] use test stagnation conditions of 1.44E + 01 psia and 7.70E + 01 F, 47% higher in stagnation pressure than the experiments but with the same stagnation temperature. Therefore, the actual bow-shock offset seen during the experiments was less than that shown in Fig. 14 and within (but very close to) the limits of the phase modulator. In Fig. 15, the simulated LDI optical path differences computed from Dunn's data are plotted for the beam locations mentioned previously. In Fig. 16, the earlier experimental

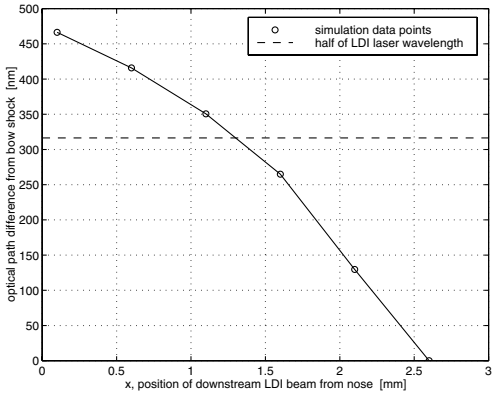

Fig. 14 Simulated bow-shock-induced optical path difference between LDI beams.

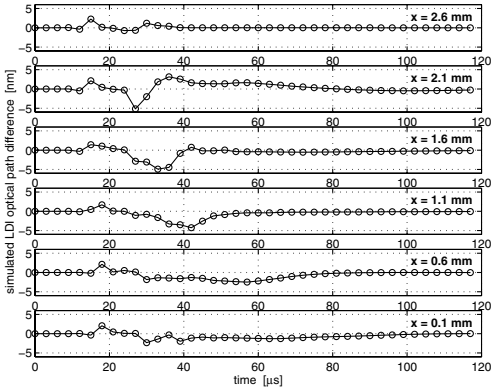

Fig. 15 Survey of simulated LDI optical path differences reduced from Dunn's [18] CFD data.

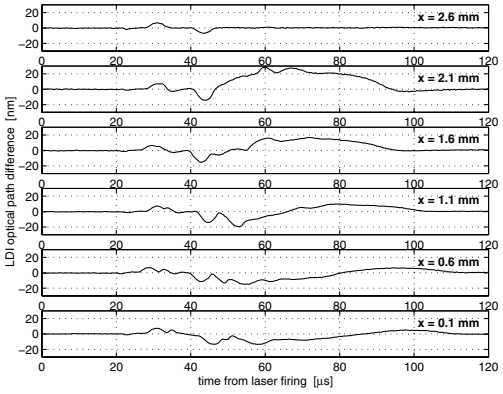

Fig. 16 Survey of actual LDI optical path differences.

LDI results [20] are shown. Besides the mismatched stagnation pressure between the experiment and the CFD simulation, the perturbation in the simulation was also introduced closer to the model than in the actual experiments. As such, the responses come sooner in the simulated results of Fig. 15. In addition, the hot-spot perturbation in the CFD simulation was modeled as an energy pulse in the computational grid along the stagnation streamline in the flow, with no modeling of the surrounding weak shock.

Figures 15 and 16 show the same general trends. The hot spot first crossing the reference LDI beam in the freestream is visible in both plots. The strong negative peaks that occur earlier, farther away from the nose, are present in the CFD results. The strong positive peaks that also occur earlier, farther away from the nose, are also present in the CFD results, with their magnitudes increasing in unison with the experimental results. One of the biggest discrepancies between the two results is the smaller optical path difference computed from the CFD simulation. Dunn [18] suspected that the discrepancies in his results were from poor resolution in the hot-spot simulation.

Another cause of error in the comparison with the CFD results may be the temporal resolution of the CFD data. Each time step in the CFD simulation is 3 μs. Perhaps with better time resolution, some of the higher-frequency features within the experimental results could be matched. The comparison makes clear that the most significant needed improvement to CFD simulation and modeling of the experiments would be an improved model of the perturbation. Specifically, an accurate density profile and improved resolution of the evolution of the hot spot. The numerical simulation of the perturbation presented in this paper should be a valuable tool to those seeking to validate unsteady hypersonic CFD codes by comparing with LDI measurements in high-speed receptivity experiments [19,20].

V. Conclusions

A numerical simulation of a controlled, repeatable, laser-generated perturbation has been presented that generates an accurate model of the hot spot and surrounding weak shock that comprise the perturbation. Not only does this result characterize the perturbation used in earlier high-speed receptivity experiments [19,20], but the density profile of the perturbation and its evolution provide an accurate model for input into CFD codes that attempt to simulate the experiments for validation purposes.

With an accurate model of the perturbation, it is hoped that future CFD simulations will generate results similar to the benchmark data from the LDI receptivity experiments [19,20].

Acknowledgements

The work was supported in part by the U.S. Air Force Office of Scientific Research under grant F49620-97-1-0037. G. Smeets and F. George of the French–German Research Institute (ISL), Saint-Louis, France provided helpful suggestions, dissemination of LDI knowledge, and time with the author for demonstration of the early LDI setup.

References

[1] Schneider, S. P., "Hypersonic Laminar-Turbulent Transition on Circular Cones and Scramjet Forebodies," *Progress in Aerospace Sciences*, Vol. 40, Nos. 1–2, 2004, pp. 1–50.

[2] Saric, W. S., Reed, H. L., and Kerschen, E. J., "Boundary-Layer Receptivity to Freestream Disturbances," *Annual Review of Fluid Mechanics*, Vol. 34, 2002, pp. 291–319.

[3] Kovasznay, L. S. G., "Turbulence in Supersonic Flow," *Journal of the Aeronautical Sciences*, Vol. 20, Oct. 1953, pp. 657–682.

[4] Mckenzie, J. F., and Westphal, K. O., "Interaction of Linear Waves with Oblique Shock Waves," *Physics of Fluids*, Vol. 11, No. 11, Nov. 1968, pp. 2350–2362.

[5] Maslov, A. A., Shiplyuk, A. N., Sidorenko, A. A., and Arnal, D., "Leading-Edge Receptivity of a Hypersonic Boundary Layer on a Flat Plate," *Journal of Fluid Mechanics*, Vol. 426, Jan. 2001, pp. 73–94.

[6] Egorov, I. V., Fedorov, A. V., and Nechaev, A. V., "Receptivity of Supersonic Boundary Layer on a Blunt Plate to Acoustic Disturbances," AIAA Paper 2004-0249, 2004.

[7] Zhong, X., "Leading-Edge Receptivity to Free-Stream Disturbance Waves for Hypersonic Flow over a Parabola," *Journal of Fluid Mechanics*, Vol. 441, Aug. 2001, pp. 315–367.

[8] Zhong, X., and Lee, T. K., "Nonequilibrium Real-Gas Effects on Bowshock/Disturbance Interaction in Hypersonic Flow Past a Cylinder," AIAA Paper 96-1856, 1996.

[9] Schneider, S. P., "Effects of High-Speed Tunnel Noise on Laminar-Turbulent Transition," *Journal of Spacecraft and Rockets*, Vol. 38, No. 3, May–June 2001, pp. 323–333.

[10] Schmisseur, J. D., Collicott, S. H., and Schneider, S. P., "Laser-Generated Localized Freestream Perturbations in Supersonic and Hypersonic Flows," *AIAA Journal*, Vol. 38, 4, Apr. 2000, pp. 666–671.

[11] Hussaini, M. Y., and Erlebacher, G., "Interaction of an Entropy Spot with a Shock," *AIAA Journal*, Vol. 37, No. 3, Mar. 1999, pp. 346–356.

[12] Fabre, D., Jacquin, L., and Sesterhenn, J., "Linear Interaction of a Cylindrical Entropy Spot with a Shock," *Physics of Fluids*, Vol. 8, No. 13, Aug. 2001, pp. 2403–2422.

[13] Federov, A., and Tumin, A., "Initial-Value Problem for Hypersonic Boundary-Layer Flows," *AIAA Journal*, Vol. 41, No. 3, Mar. 2003, pp. 379–389.

[14] Stetson, K. F., "Boundary-Layer Transition on Blunt Configurations," NASA Johnson Space Center, Rept. JSC-26528, Feb. 1994; also Lockheed Engineering and Sciences Co., Rept. LESC-31143, Houston, TX.

[15] Morkovin, M. V., "Note on the Assessment of Flow Disturbances at a Blunt Body Traveling at Supersonic Speeds Owing to Flow Disturbances in Free Stream," *Journal of Applied Mechanics*, Vol. 27, No. 2, June 1960, pp. 223–229.

[16] Kruse, R. L., "Transition and Flow Reattachment Behind an Apollo-Like Body at Mach Numbers to 9," NASA TN-D-4645, July 1968.

[17] Schneider, S. P., Collicott, S. H., Schmisseur, J. D., Ladoon, D., Randall, L. A., Munro, S. E., and Salyer, T. R., "Laminar-Turbulent Transition Research in the Purdue Mach-4 Quiet-Flow Ludwieg Tube," AIAA Paper 96-2191, 1996.

[18] Dunn, J. W., "Numerical Simulation of Bow-Shock/Disturbance Interactions in Mach-4 Flows Past a Hemisphere," AIAA Paper 98-0007, 1998.

[19] Salyer, T. R., Collicott, S. H., and Schneider, S. P., "Feedback Stabilized Laser Differential Interferometry for Supersonic Blunt Body

Receptivity Experiments," AIAA Paper 2000-0416, 2000.
[20] Salyer, T. R., Randall, L. A., Collicott, S. H., and Schneider, S. P., "Use of Laser Differential Interferometry to Study Receptivity on a Hemispherical Nose at Mach 4," AIAA Paper 98-0238, 1998.
[21] Schneider, S. P., and Haven, C. E., "Quiet-Flow Ludwieg Tube for High-Speed Transition Research," *AIAA Journal*, Vol. 33, No. 4, Apr. 1995, pp. 688–693.
[22] Bushnell, D. M., *Notes on Initial Disturbance Fields for the Transition Problem*, edited by M. Y. Hussaini and Voigt, R. G., Instability and Transition, Vol. 1, Springer–Verlag, Berlin, 1990, pp. 217–232.
[23] Reshotko, E., "A Program for Transition Research," *AIAA Journal*, Vol. 13, No. 3, Mar. 1975, pp. 261–265.
[24] Mack, L. M., "Linear Stability Theory and the Problem of Supersonic Boundary-Layer Transition," *AIAA Journal*, Vol. 13, No. 3, Mar. 1975, pp. 278–289.
[25] Yan, H., Adelgren, R., Elliott, G., Knight, D., Boguszko, M., Ivanov, M., Kudryavtsev, A., and Khotyanovsky, D., "Laser Energy Deposition in Quiescent Air," AIAA Paper 2003-1051, 2003.
[26] Collicott, S. H., Messersmith, N. L., and Schneider, S. P., "Review of Optical Diagnostic Methods for Hypersonic Quiet-Flow Ludweig Tube Facilities," AIAA Paper 96-0851, 1996.
[27] Smeets, G., "Interferometry," Institut Franco-Allemand de Recherches de Saint-Louis, Rept. CO 214/90, Saint-Louis, France, 1990.
[28] Salyer, T. R., "Laser Differential Interferometry for Supersonic Blunt Body Receptivity Experiments," Ph.D. Thesis, School of Aeronautics and Astronautics, Purdue Univ., West Lafayette, IN, May 2002.
[29] Smeets, G., "Flow Diagnostics by Laser Interferometry," *IEEE Transactions on Aerospace and Electronic Systems*, Vol. AES-13, No. 2, Mar. 1977.
[30] Smeets, G., and George, A., "Laser-Interferometer with Phase Compensation," Institut Franco-Allemand de Recherches de Saint-Louis, Rept. R136/75, Saint-Louis, France, Dec. 1975; also Defense Technical Information Center Citation AD-A307548, Oct. 1995.
[31] Mcguire, J. B., "Fluid Dynamic Perturbations Using Laser-Induced Breakdown," Master's Thesis, School of Aeronautics and Astronautics, Purdue Univ., West Lafayette, IN, Aug. 1994.
[32] Schneider, S. P., Mcguire, J. B., Collicott, S. H., and Salyer, T. R., "Laser-Generation of Controlled Localized Perturbations for Boundary-Layer Transition Research," *ICIASF '95 Record*, No. 95ch3482-7, Institute of Electrical and Electronics Engineers, New York, 1995.
[33] Schmisseur, J. D., "Receptivity of the Boundary Layer on a Mach-4 Elliptic Cone to Laser-Generated Localized Freestream Perturbations," Ph.D. Thesis, School of Aeronautics and Astronautics, Purdue Univ., West Lafayette, IN, Dec. 1997.
[34] Sedov, L. T., *Similarity and Dimensional Methods in Mechanics*, Academic Press, New York, 1959.

S. Aggarwal
Associate Editor